Experimental Investigation of Discharge Plasma Magnetic Confinement in the NSTAR Ion Thruster

Anita Sengupta[*], Dennis Fitzgerald[†], Al Owens[‡]

Jet Propulsion Laboratory, California Institute of technology, Pasadena, CA, 92780

Magnetic confinement studies were performed on the state-of-the-art NSTAR ion thruster. The goal of the experimental studies was determine the dependence of plasma confinement and plasma uniformity on the strength and shape of the imposed ring-cusp magnetic field. As a full factorial test matrix was impractical, four primary cases were investigated to parametrically determine the individual effects of adding an additional magnetic cusp, increasing the gauss level of the minimum closed magnetic contour line, and varying the magnetic field free volume in the discharge chamber. A laboratory model NSTAR engine was retrofitted with additional magnets to allow experimental investigation of both enhanced 3 and 4 ring cusp geometries. The performance of each configuration was determined from bulk discharge electrical parameter measurements as well as Langmuir probe sweeps throughout the interior of the discharge chamber allowing determination of variation in plasma potential, electron temperature, electron density, and ion density. The results of the study confirm that increasing the value of the minimum closed magnetic contour line throughout the chamber significantly reduces ion loss to the anode walls. Similarly, increasing the total field free volume in the near-grid region improves plasma uniformity, removing the characteristic NSTAR on-axis current density peak, that was responsible for significant on-axis accelerator grid erosion[1]. The major finding of the study is that by reducing ion loss to the anode walls, the discharge power requirement to produce and extract beam ions from the thruster, is significantly reduced. The enhanced 3 and 4 ring cusp geometries designed and tested, resulted in a 20% reduction in discharge loss and discharge current at the NSTAR TH15 throttle point, with similar efficiency gains at half power (TH8) and minimum power (TH0) operation. In addition to improving overall electrical efficiency, the reduction in discharge power from the hollow cathode and reduction in peak current density in the beam, can significantly increase total throughout per NSTAR engine by reducing wear mechanisms that limit thruster life.

Nomenclature

V_D	=	Discharge Voltage
J_D	=	Discharge Current
ε_B	=	Discharge Loss
J_B	=	Beam Current
V_B	=	Beam Voltage
T_e	=	Electron Temperature
n_e	=	Electron Density
n_i	=	Ion Density
V_p	=	Plasma Potential
j_i	=	Ion Current Density
$I_{sati,e}$	=	Saturation current (ion , electron)
A_p	=	Probe Area

[*] Senior Engineer, Advanced Propulsion Technology, 4800 Oak Grove Drive, MS125-109, Pasadena, CA, 92780.
[†] Staff Engineer, Advanced Propulsion Technology, 4800 Oak Grove Drive, MS125-109, Pasadena, CA, 92780.
[‡] Senior Technician, Advanced Propulsion Technology, 4800 Oak Grove Drive, MS125-109, Pasadena, CA, 92780.

I. Introduction

ION engines offer the potential for orders of magnitude performance improvement over traditional chemical propulsion systems, resulting in shorter trip times, reduced launch vehicle costs, and with the push for the Nuclear Electric Propulsion (NEP) Mission Architecture, far more ambitious science return than ever before. In spite of the tremendous advantages the technology offers, actual use of the state-of-the-art ion thruster technology on NASA science missions has been limited, due to its marginal electrical efficiency, high fabrication and test costs, and reliability/lifetime issues. Significantly improving the ion thruster's efficiency and lifetime, is therefore necessary to ensure continued use of this technology on NASA science missions. The current inefficiencies of the state-of-the-art ion engine are directly related to the production and confinement of the discharge plasma in the engine's discharge (ionization) chamber. In the current configuration, for every 15A of electron current generated by the hollow cathode, only 1.76 A of ions are actually extracted through the optics assembly, to produce thrust. This is largely due to direct loss of ions to the anode walls, where they recombine with the surface. Therefore all the energy that was expended in creating an ion that is lost to the walls, is wasted. Discharge loss is defined as the ratio of the discharge power to beam current, and is typically expressed in units of eV per ion or W/A.

$$\varepsilon_B = \frac{V_D J_D}{J_B}$$

Reducing discharge loss not only increases total thruster efficiency, it also has lifetime implications. A reduction in discharge loss is simply a reduction in the discharge power or discharge current through the hollow cathode assembly. By reducing the fraction of ions that are lost to the walls, fewer ions need to be produced and therefore fewer electrons are needed to make them. As cathode emitter lifetime has an exponential dependence on current density, reducing the discharge current by 20% can increase the emitter life by up to 45%, for the NSTAR TH15 throttle point[2]. Similarly, reducing the peak current density of beam ions by improving radial plasma uniformity can increase total propellant throughput, as grid life is limited by accelerator grid erosion, which is linearly proportional to beam current density[3].

The objective of this research was to use a combined approach of analytical model development of the discharge plasma in conjunction with spatially resolved experimental measurements inside of an operating ion thruster, to quantitatively understand and improve upon the confinement and production of the discharge plasma. The experimental investigations, the subject of this paper, include bulk electrical parameter measurements of discharge current, discharge voltage, and beam current to measure the discharge loss of each configuration tested, as well as langmuir probe traces inside of an operating 30-cm diameter NSTAR thruster, to map out the plasma structure and its confinement. The end result of the research activity was to experimentally validate an enhanced NSTAR thruster design that improves ionization efficiency by 20% and plasma uniformity by 25%, significantly increasing the efficiency and lifetime of the NSTAR thruster. We have therefore demonstrated that improving the performance and throughput of the NSTAR thruster can be easily accomplished via a straightforward change in the magnetic field.

II. Experimental Setup

All experiments were performed on a laboratory model NSTAR engine, referred to as the NKO1 thruster (Figure 1). The NKO1 engine and flight NSTAR engine, are functionally identical and a performance comparison of the laboratory model and flight spare NSTAR engine (FT2) is documented in Table 2. All engine tests were performed in the Jet Propulsion laboratory's Endurance Test Facility (Figure 2). The 3-m-diameter by 10-m-long vacuum chamber provides a base pressure of 1×10-5 Pa (1×10-8 Torr) and about 5×10-4 Pa (4×10-6 Torr) at the NSTAR full-power flow rates. The propellant-feed system consisted of two Unit Instruments mass flow meters in each of the main, cathode, and neutralizer flow lines. The main flow meter had a range of 0 to 100 sccm and the cathode flow meters had a 0- to 5 sccm range. Laboratory power supplies with similar capabilities to the DS1 flight power-processing unit (PPU) were used to run the NKO1 engine. A Labview-based computer data acquisition and control system was used to monitor engine electrical parameters as well as control the power supplies. High-voltage signal

Figure1. NKO 1 Ion Thruster

isolation was provided by fiber optic transmission lines to transfer 0-5V signals between the grounded DAQ system and the high voltage engine output and supplies.[1]

The NKO1 engine was configured to allow the translation of up to seven Langmuir probes providing radial plasma parameter profiles from the anode wall to just past the thruster centerline for both the cylindrical and conical chamber regions (Figure 3). Seven 0.75 cm diameter holes were cut into the anode wall to allow the translation of various probes. The probe locations provided a spatially resolved discharge plasma characterization, from 1 cm to 14 cm downstream of the discharge cathode keeper (2 cm upstream of the screen grid), in the axial direction. The axial locations of the probes were 1, 2 , 3, 4, 6, 10, and 14 cm downstream of the keeper electrode (Figure 4). Higher spatial resolution was required in the near keeper plasma as density and potential gradients are known to be highest in the vicinity of the cathode[4.] The probes were inserted into and retracted from the discharge chamber by a high speed linear translation stage (Figure 3). The computer controllable lead screw driven stage was able to operate at a variety of speeds, with a maximum speed of 50.8 cm/sec. This enabled a 16.5cm probe insertion and retraction operation to be less than 0.8 sec. There was a 0.1 sec dwell period between the insertion at 16.5 cm and the subsequent retraction A sample translation profile in shown is Figure 6. Position relative to home was recorded with a linear position transducer. The probes were mounted to the stage on the probe mount shown in Figure 3 Teflon spacers and setscrews were used to hold the alumina tube probes in a fixed position on the probe mount. Alignment and insertion into the engine was accomplished by a thruster probe mount, which housed each probe in stainless steel collar inserted into the anode wall that protruded up to 0.76 cm into the discharge chamber (Figure 4).[5]

Flat plate Langmuir probes were used to eliminate the effect of radial sheath expansion that prevented electron saturation of cylindrical probing in the low density region of the discharge chamber studied previously[5]. Although a sheath still forms around a flat disc probe, the expansion is perpendicular to the surface of the disk, and therefore does not increase the total probe collection area. As the aspect ratio (D/t) of the disc is 100, end effects are assumed to be negligible. Each probe consisted of a 0.4 cm diameter tungsten disk spot welded to at 0.05 cm diameter Ta wire, that was fed through first a single bore alumina tube with a 0.1 cm OD inserted into a single bore ceramic with a 0.48 cm OD (Figure 7). This dual-ceramic, necked down configuration was chosen to minimize perturbations due to insertion of a large insulating surface into the plasma. The Ta wire extended 8 to 10 cm beyond the ceramic and mated to a flexible copper wire 10 to 20 cm in length to minimize torsional loads on the comparatively rigid Ta wire. The position of the Ta wire inside the ceramic tube, was maintained with several layers of high temperature shrink tubing affixed at the end of each alumina rod. The copper wire was fitted with coax connection to electrically connect each probe to the junction box. Each langmuir probe coax output connection was fed into a shielded junction box (Figure 3). The junction box could take up to 5 probe electrical connections. The output signals from the junction box were routed through the vacuum chamber to a combination of ISI SHV10 and standard coaxial vacuum feedthroughs. The ISI feedthroughs were rated to 10kV isolation with respect to ground, and the standard coaxial feedthroughs were rated to 2kV isolation. The vacuum feedthroughs and the air-side cabling shields were electrically connected facility ground to reduce signal noise.

A separate LABVIEW data acquisition system was used to control the translation stage, probe power supplies, and record current/voltage data from each probe. A high-speed data acquisition card, with a sampling rate of up to 2 MHz for analog input and 1kHz for analog output was used to record current-voltage waveform data. A bipolar power supply was used to bias the Langmuir probes +/- 50V with respect to cathode common. The voltage waveform was a saw tooth ramp, cycled at 10-100 Hz typically for a duration of 1 to 3 seconds. The bias supply was placed in series with the probe and cathode common, and allowed to float at the thruster potential with respect to ground. As the data acquisition system was at ground potential, and the thruster operating up to 1100 V above ground potential, it was necessary to isolate the probe signal and control voltage for the bias power supply. This was accomplished via the use of two fiber optic link modules. Each module either receives from or transmits to the complementary module, optically, a via linear 0-5V signal. The current through each probe was measured across a 1-Ohm current shunt. The voltage output from the shunt was conditioned using a low-pass RC filter circuit, and then routed through the fiber optic link module, to be read by the grounded data acquisition system. The control voltage for the bias supply was transmitted in the reverse manner from ground to high voltage through the fiber optic link module. High voltage and ground potential equipment were physically isolated from each other using fiberglass and g10 boards mounted in a standard rack. AC power was provided to the floating bias supply through a 10kV isolation transformer with the high voltage side referenced to cathode common.

Figure 2. Endurance Test Facility at the Jet Propulsion Laboratory.

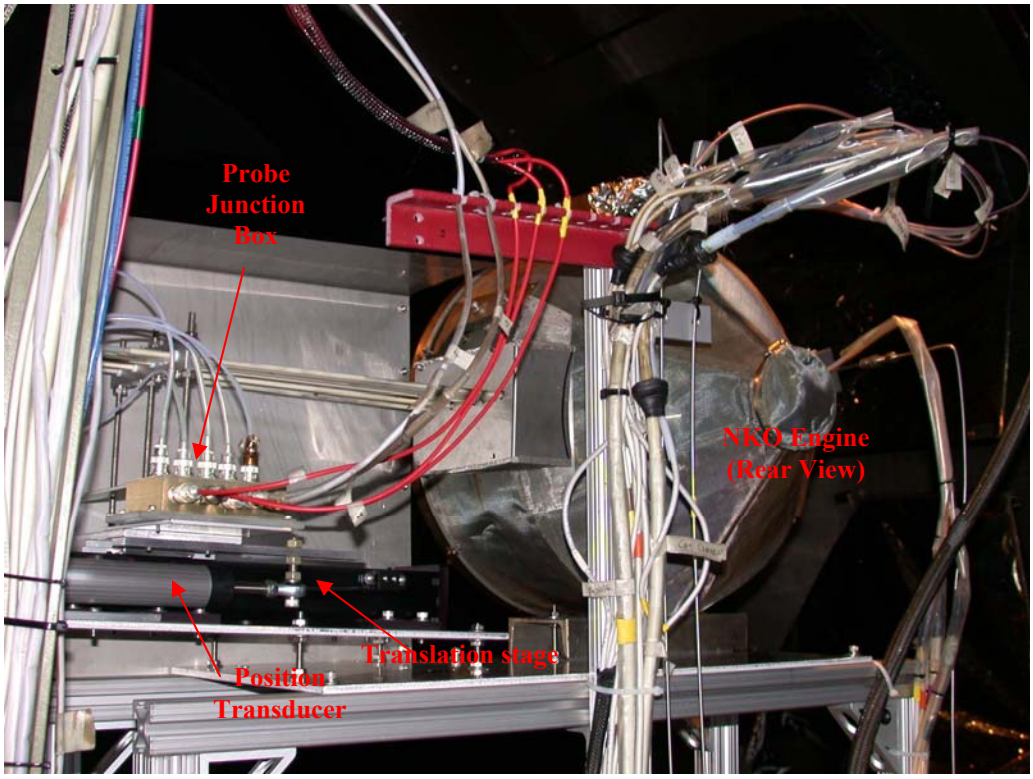

Figure 3. NKO1 in the Endurance Test Facility at the Jet Propulsion Laboratory.

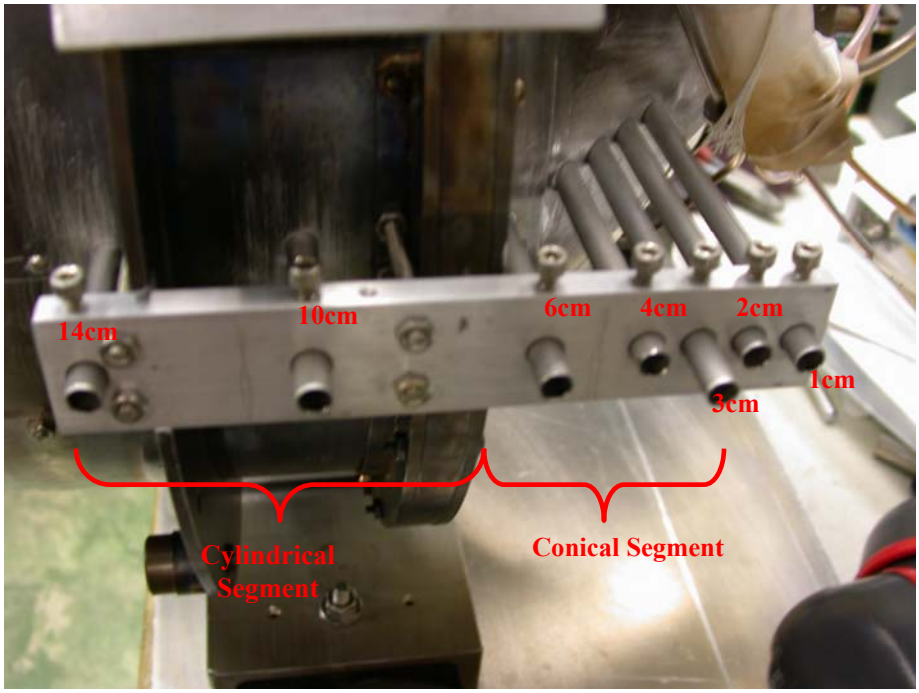

Figure 4. Seven Axial probe locations as seen from outside the NKO engine).

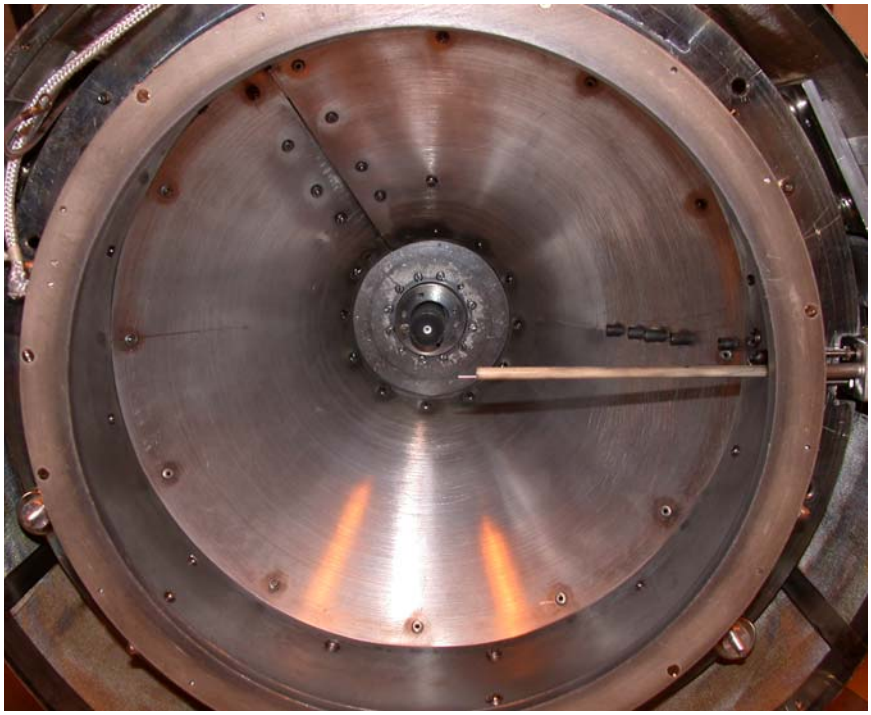

Figure 5. Seven Axial probe locations as seen from inside the NKO engine (optics removed).

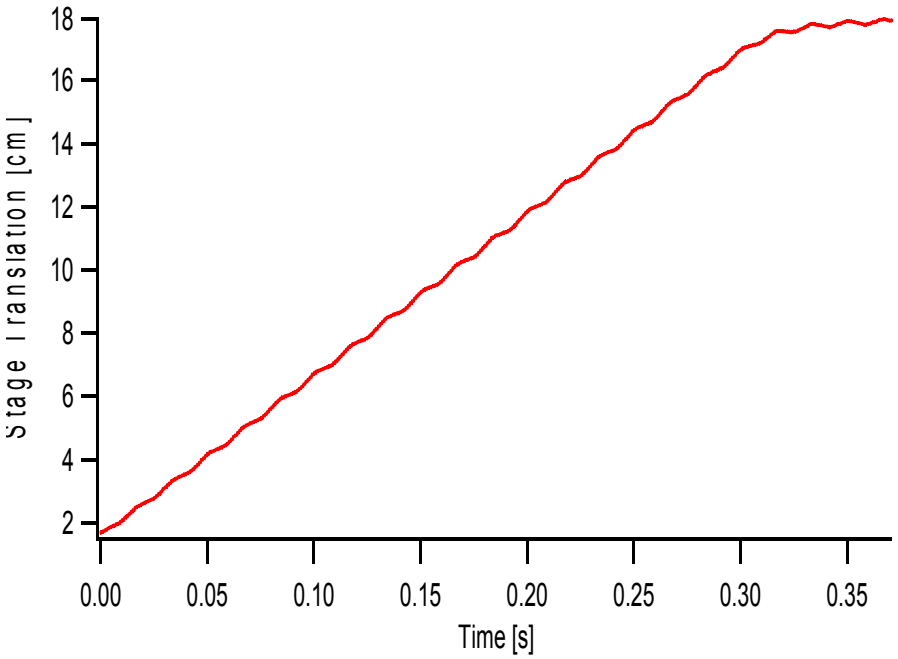

Figure 6. Typical Translation Profiles versus time.

Figure 7. Flat Disk Langmuir Probe.

III. Experimental Results

A. Summary of Experimental Studies

VERSION	NUMBER OF MAGNET RINGS	CONTOUR LINE CLOSURE (G)
V1 (Nominal)	3	20
V2	4	30
V3	4	50
V4	3	50

Table 1. Summary of NSTAR Engine Tests

Bulk performance and plasma parameter measurements for four separate NSTAR thruster magnetic field configurations were obtained. For each case, the NKO1 thruster was physically modified by the addition/replacement of permanent magnets. The goal of the magnetic studies was determine the dependence of plasma confinement and plasma uniformity on the strength and shape of the imposed ring-cusp magnetic field. Four primary cases were investigated to parametrically determine the individual effects of the following:

1. Adding an additional cusp
2. Increasing the gauss level of the minimum closed contour line
3. Varying the magnetic field geometry with respect to the anode wall.

Table 1 is a summary of the magnetic configurations tested. For each of these cases, a 2D map of the magnetic field and magnetic contours was computed with the software MAXWELL 2D. The test sequence was then to retrofit NKO1 for the new magnetic circuit, measure the individual cusp magnetic field strengths with a gauss meter, and then install the engine in the test facility for experimentation.

B. Nominal NSTAR Results: Case V1

1. Overall Performance

DISCHARGE PARAMETER	NKO1 (V1)			FT2 (BOL)		
	TH15	TH8	TH0	TH15	TH8	TH0
J_B (A)	1.76	1.10	0.51	1.76	1.10	0.51
J_D (V)	14.8	8.3	5.3	14.3		5.3
V_D (V)	24.65	26.2	25.70	24.7		25.5
ε_b (V)	207.3	197.7	267.1	201		267
η_{tot}	0.62		0.42	0.62		0.41

Table 2. Nominal (v1) NKO1 and FT2 Performance (1khrs)[6].

The performance as a function of runtime and power level, of the nominal NSTAR thruster, is well documented in references 1 and 5. Table 5-2 compares the performance of the nominal NKO1 and FT2 engine after 1000 hours of operation. Discharge power varies with thruster wear, as erosion of the accelerator grid hole pattern leads to increased neutral loss[6]. Therefore the 1,000 hour mark for FT2 operation from the ELT, was chosen as a representative point for comparison between the engines, as they exhibited a similar degree of accelerator grid wear. Performance data is presented for TH15, TH8, and TH0 operation. As can be seen, the laboratory model engine is not identical but certainly representative of the flight thruster performance. Variances between the two can be related to minor differences in the axial cathode location and nominal grid gap of the optics assembly.

Figure 8 and 9 are MAXWELL 2D plots of lines of constant magnetic strength and the magnetic field lines. From these plots we can see that the nominal thruster configuration closes only the 20G contour line and the field free volume in the cylindrical segment is significantly smaller than the physical volume. Although the cusp strength

is sufficiently high to minimize primary electron loss, it is likely that secondary electrons and therefore ions are not well confined due to the weak magnetic field.

NSTAR Throttle Level	Nominal Thruster Power	Beam Supply Voltage	Beam Current	Accelerator grid Voltage	Neutralizer Keeper Current	Main Flow	Discharge Cathode Flow	Neutralizer Cathode Flow
	kW	V	A	V	A	sccm	sccm	sccm
TH 0	0.52	650	0.51	-150	2.0	5.98	2.47	2.40
TH 8	1.46	1100	1.1	-180	1.5	14.41	2.47	2.40
TH15	2.33	1100	1.76	-180	1.5	23.43	3.70	3.60

Table 3. Subset of the NSTAR Throttle Table[1].

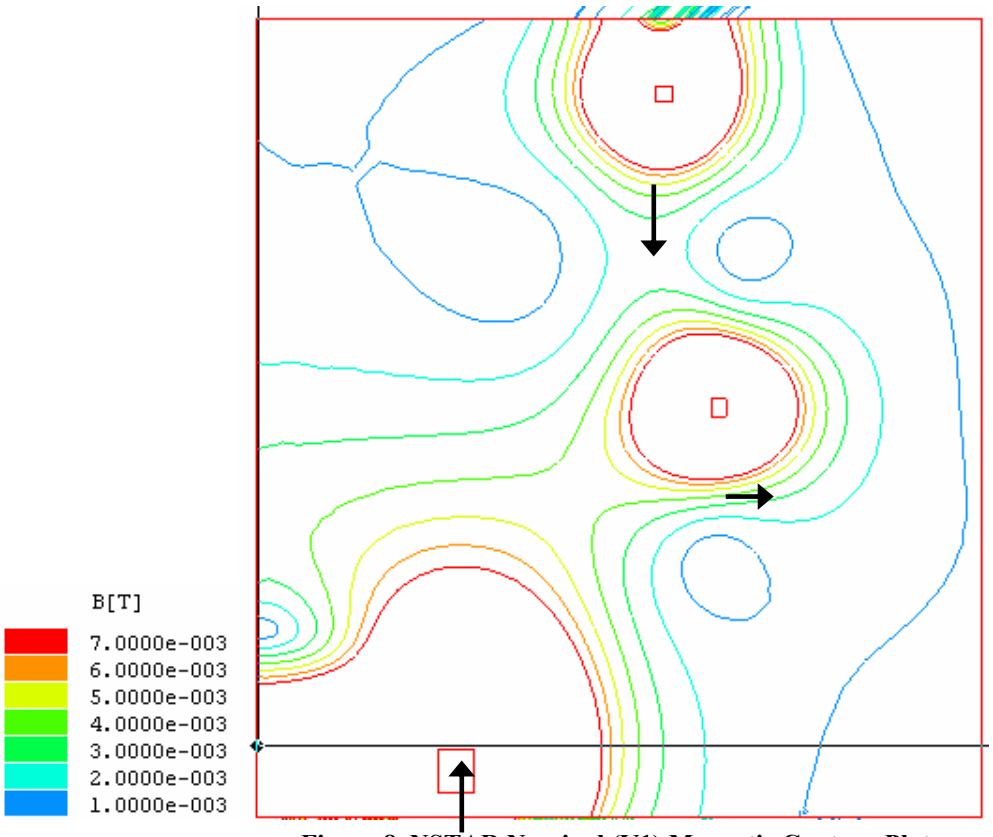

Figure 8. NSTAR Nominal (V1) Magnetic Contour Plot.

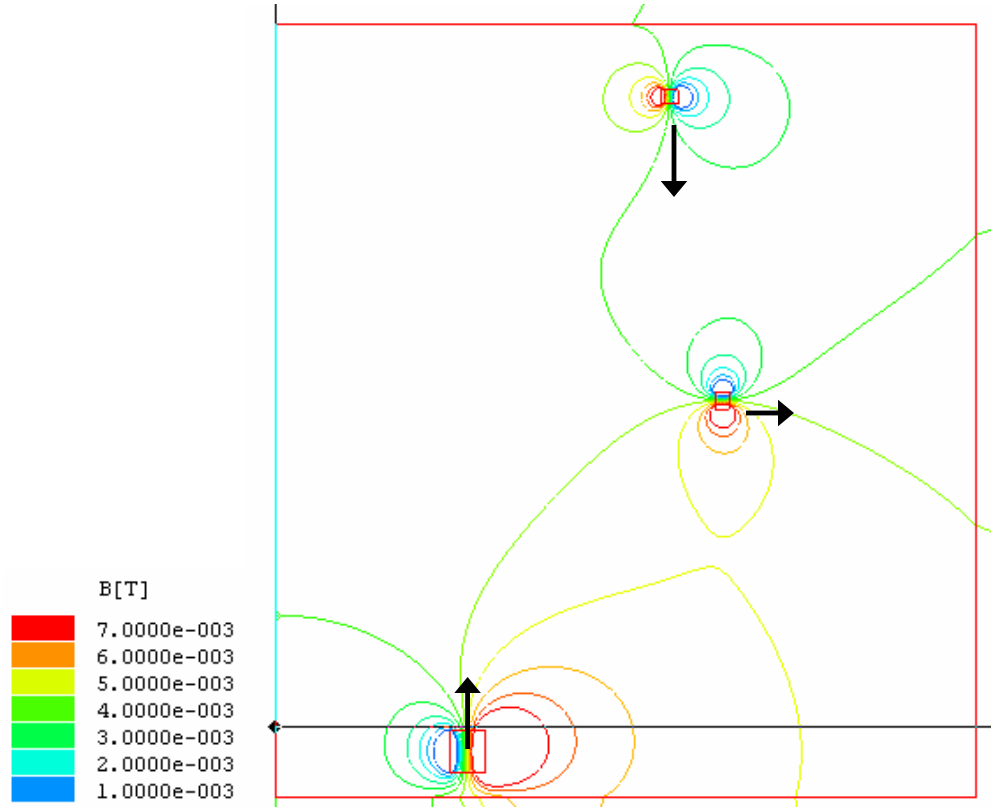

Figure 9. NSTAR Nominal (V1) Magnetic Field Lines.

2. Plasma Profiles

A total of 7 flat disc probes were used in the investigation of the nominal thruster configuration. The axial locations of the cylindrical probes were 1, 2, 3, 4, 6, 10, and 14 cm downstream of the keeper electrode. The region from 1cm to 6 cm downstream of the keeper is the conical portion of the chamber The region from 10 to 14 cm downstream of the keeper is the cylindrical portion of the chamber. The 14cm location is located just upstream of the screen, and is used to determine the representative beam profile for each configuration. Figures 10 though 13 present radial variation in electron number density, electron temperature, and plasma potential for each axial probe location at the TH15 operating point. TH15 operation is defined by the beam voltage, beam current, and flow rates in table 3. Electron number density data is shown from the anode wall to just past the centerline, to illustrate the symmetry and peaked nature of the plasma. However, electron temperature and plasma potential calculation were only made up to the thruster centerline, as passage of the alumina tubes in front of the cathode tended disturbed its operation. Figure 10 is the electron number density radial variation. Electron number density was reduced from the electron temperature and electron saturation current measurements, both of which were obtained from the current voltage traces by the method described in reference 7.

$$n_e = \frac{4I_{sat}}{A_p e\sqrt{\frac{8kT_e}{\pi m_e}}}$$

In the conical region of the discharge chamber, electron number density was found to be peaked on the centerline at a maximum 1e12 cm^{-3} 1 cm downstream of the cathode, and decreased rapidly in the radial direction to a minimum of 4e10 cm^{-3}, near the anode wall consistent with other researchers in the field[4,8]. This structure is consistent with a high density cathode plume typical of hollow cathode discharge plasma. In the cylindrical region of the discharge chamber, radial variation in density was not as peaked, and varied radially from 4e11 cm^{-3} to 1e11 cm^{-3} at the anode wall. Density gradients in both the radial and axial direction decreased in magnitude with distance from the cathode. In figure 5-11, the radial variation, in electron temperature was similarly peaked. In the conical segment it spanned from a maximum of 5.75 eV on the centerline, to a minimum of 1.5 eV at the anode wall. Radial variation, in the

cylindrical segment spanned 4.75 to 3 eV, with the maximum on the centerline, and minmum at the anode wall. Electron temperature measurements have an uncertainty band of $\pm$0.5eV, mainly a result of the maxwellian exponential fitting process as the plasma was not purely maxwellian. Figure 5-13 is the plasma potential variation, determined as the voltage corresponding to the maximum of the first derivative of the probe trace as discussed in reference 9. The uncertainty in the plasma potential measurement is $\pm$2V due to the error induced from taking the derivative of a relatively noisy probe trace. Plasma potential was highly peaked on axis from 2 to 14cm downstream of the cathode. Axial variation is this region was from 26 to 32V, increasing in the downstream direction. Radial variation was from a maximum 32 at 10cm downstream on axis to 25V in the vicinity of the anode wall in both the cylindrical and conical region of the plasma. The plasma potential measurement made at 1 cm downstream of the keeper, was not peaked, however. At 1 cm downstream, the plasma potential was 24.4V on axis and increased radially to 26.6V at the anode wall. Similar to the electron temperature and density, the gradient in radial variation decreased in the downstream direction, consistent with a more uniform plasma with distance from the cathode.

Figure 5-14 represents the variation in ion saturation current density throughout the discharge chamber. Ion saturation current measurements were made by biasing each probe 25V negative of cathode common potential, to repel all electrons and collect only ions.

$$j_i = \frac{I_{sat,i}}{A_p}$$

With knowledge of the electron temperature, and the assumption that ions are collected by the probe at the bohm velocity, the ion density can also be calculated[10].

$$n_i = \frac{j_i}{e\sqrt{\frac{kT_e}{m_i}}}$$

The ion density was highly peaked on axis, in the conical section of the discharge chamber, suggesting that most of the ionization in the nominal configuration occurs within the cathode plume in the vicinity of the cathode. With increasing distance from the cathode the ion density became more uniform. It is also important to note that the ion density was within 10% of the measured electron density for all probe traces investigated, confirming that ions are indeed electrostatically confined by the plasma electrons.

In general, the plasma parameter measurements for the nominal configuration indicate that the plasma density and temperature is peaked on axis, consistent with a high degree of ionization within the cathode plume, resulting in a radially non-uniform plasma. Radial gradients in both electron density and electron temperature were less significant in the cylindrical region of the chamber, therefore. The beam profile, defined by the ion saturation probe trace at 14cm downstream of the cathode, was highly peaked on axis, consistent with faraday probe traces taken in reference 6. The plasma potential was also highly peaked on axis (within the cathode plume) from 2 cm to 14 cm downstream of the cathode. Outside of the cathode plume the radial potential variation was monotonic approaching the discharge voltage at the anode wall, in both the cylindrical and conical region of the chamber. At 1 cm downstream of the cathode, however, the plasma potential was depressed on axis, and increased in value with proximity to the anode wall.

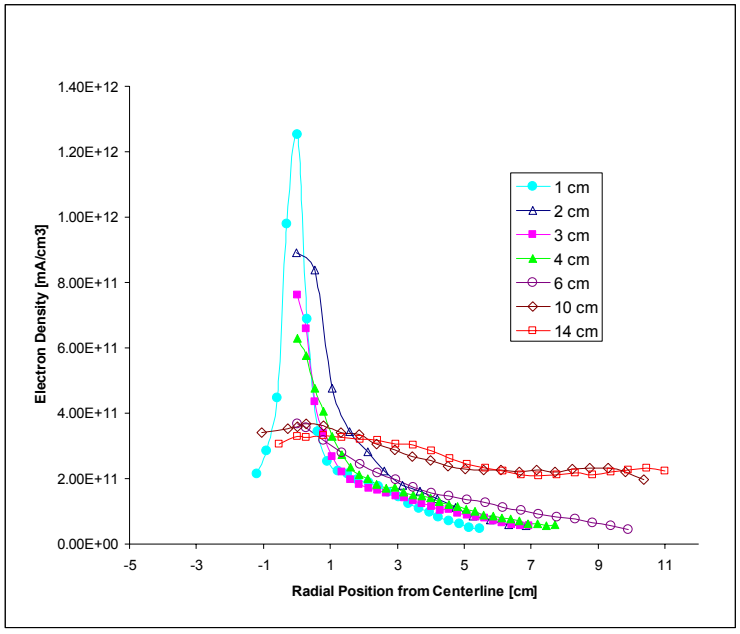

Figure 10. Electron Number Density Profiles at TH15 for V1 Configuration.

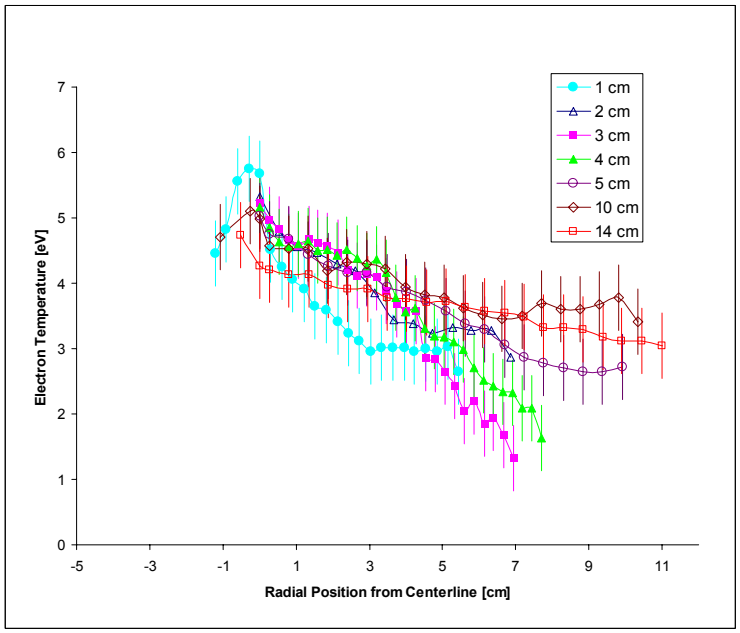

Figure 11. Electron Temperature Profiles at TH15 for V1 Configuration.

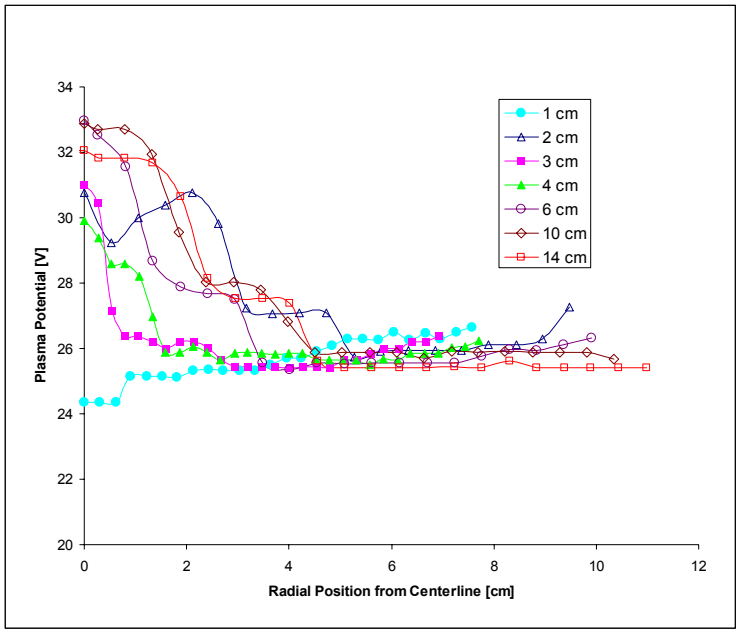

Figure 12. Plasma Potential Profiles at TH15 for V1 Configuration.

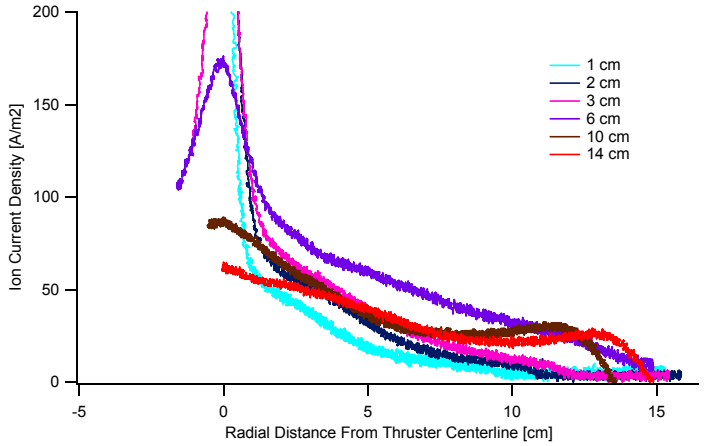

Figure 13. Ion Saturation Current Density Profiles at TH15 for V1 Configuration.

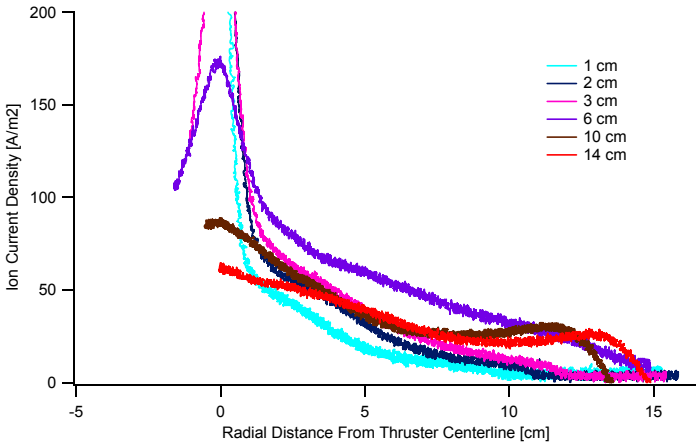

Figure 14. Ion Number Density Profiles at TH15 for V1 Configuration.

C. Enhanced 4 Ring Cusp NSTAR: Case V2

1. Overall Performance

Case 2 is a 4-ring cusp modified NSTAR engine. In this configuration, a ring of magnets was added to the center of the conical section of NKO1, with the direction of magnetization pointing into to the discharge chamber, normal to the surface of the magnet. To retain the alternating polarity cusp design, the cathode ring polarity was reversed, and the middle and front magnet rings were left unchanged. A thin steel shim was placed in the interior of the chamber to aid in the retention of magnets to the cone section. Although this aided in magnet insertion, the ferrous material resulted in a significant lowering of the cusp strength, reducing its effectiveness at confining electrons. Figure 15 and 16 are plots of the MAXWELL 2D predicted magnetic contour and field lines. Although this configuration closed the 30G contour throughout the chamber and increase the field free volume in the cylindrical segment, it did not result in a noticeable performance change over the nominal configuration (Table 4). This can be attributed to the weak cusp strength of the new conical magnet ring b/c of the steel shim used to retain the magnets. A ferrous material shunts magnetic field lines, and therefore use of the shim reduced the surface magnetic field strength. Measurement of the cusp strength with a gauss-meter revealed it was only 820G, insufficient to prevent measurable primary electron loss to the cusp. The shim was subsequently removed for case V3, and the cusp strength increased to 1800 G. V2 testing was made, however, with the shim in place.

DISCHARGE PARAMETER	NKO (V2)		
	TH15	TH8	TH0
J_B (A)	1.76	1.10	0.51
J_D (V)	14.3	8.5	5.3
V_D (V)	24.7	25.1	25.5
ε_b (V)	200.7	194.0	265.0
η_{tot}			

Table 4. Enhanced 4-Ring Cusp NSTAR Performance.

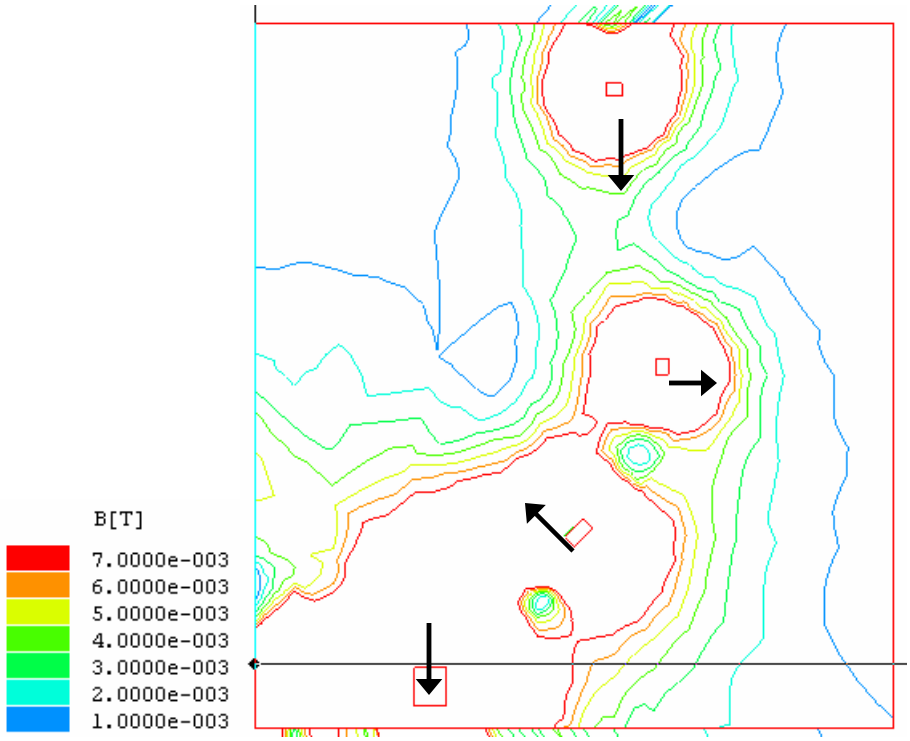

Figure 15. 4 Ring Cusp NSTAR (V2) Magnetic Contour Plot.

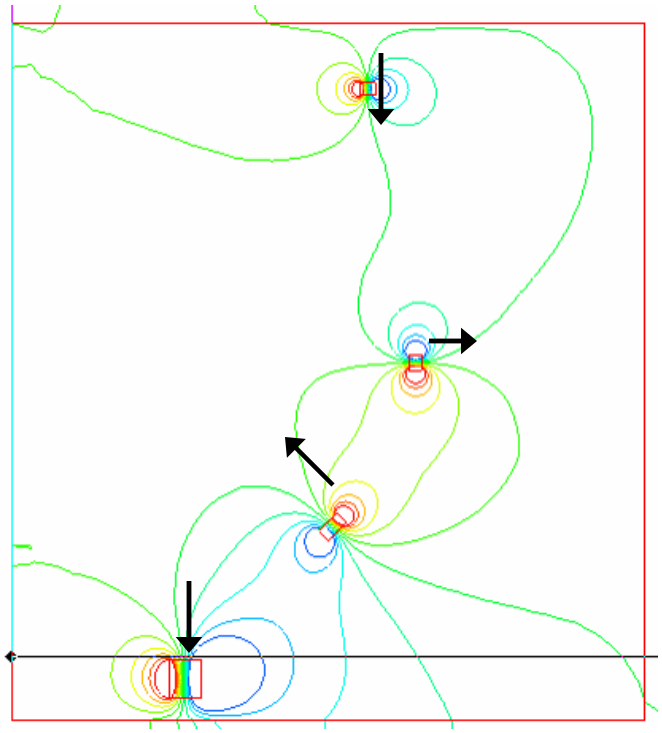

Figure 16. 4 Ring Cusp NSTAR (V2) Magnetic Field Lines.

2. Plasma Profiles

Radial plasma parameter profiles for case 2 were made with six flat disk langmuir probes located at 1cm, 3cm, 4cm, 10cm, and 14cm axially with respect to the discharge cathode exit . Figures 17 to 19 present radial variation in electron number density, electron temperature, and plasma potential, for each axial probe location at the TH15 operating point. As in the nominal case, TH15 operation is defined by the beam voltage, beam current, and flow rate setpoints in the NSTAR throttle table. Therefore changes in performance for V2 versus V1 will be limited to changes in the discharge current and voltage required to produce and extract 1.76A of beam current through the optics. All probe traces were made from the anode wall to just past the thruster centerline, identical to the nominal case. Figure 17 is a plot of the electron number density. In the conical region of the discharge chamber, the radial variation in electron density had a primary peak on the centerline, as well as a secondary peak off axis. The primary peak, on the centerline was due to the cathode plasma plume and had a maximum value of 9e11 cm^{-3}, as measured 1cm downstream of the cathode. The secondary peak was caused by the addition of the conical magnet ring, causing electrons leave the centerline axis and to travel along the new field lines to the conical magnetic cusp. The maximum number density in the secondary peak was 1.5e11 cm^{-3}, as measured 7cm radially from the centerline, by the probe 4cm axially downstream of the cathode. The radial variation of electron density in the cylindrical region of the plasma was relatively flat, confirming that a field free volume in necessary for increased plasma uniformity. Electron density varied from a maximum of 2e11 cm^{-3} on the centerline to 1.5e11 cm^{-3} near the anode wall, in the cylindrical segment. Figure 18 is a plot of electron temperature radial profiles in the discharge chamber. As with the nominal case, the uncertainty in the electron temperature calculation is $\pm$ 0.5 eV, due to the maxwellian fitting errors. The radial variation in electron temperature in the conical segment, was peaked on axis (5.2 eV), with an additional off axis peak (4.8 eV), corresponding to the electron density peaks described previously. The electron temperature reached a minimum of 2eV near the anode wall in the conical segment. Radial variation, in the cylindrical segment was less peaked, and spanned 4.5 to 3 eV, with the maximum on the centerline, and minimum at the anode wall. Figure 19 is the plasma potential variation. The plasma potential structure was varied in the conical region of the discharge chamber. In the region 1 to 3 cm downstream of the cathode, the plasma potential increased in the radial direction. The potential also exhibited a depression in potential on axis, and a large off axis peak in potential in the region of the conical magnetic cusp. At 4 cm downstream, the plasma potential was peaked on axis, leveled off to about 26V, then began to increase in the radial direction in the region corresponding to the magnetic cusp. From 10 to 14 cm downstream, there was minimal radial variation in the plasma potential, but decreased axially in value from 27.5 to 25V. Figure 20 represents the variation in ion saturation current density throughout the discharge chamber. In the conical section, ion density was highly peaked on axis, and also exhibited a secondary peak due to the new magnetic cusp. Ion density in the cylindrical segment was essentially flat from the centerline out to 13 cm radially. In fact the 14cm probe trace, which was used as the beam profile measurement for these studies, exhibited a flatness parameter of greater than 90%, largely due to the field free volume in the cylindrical segment near the grids.

The plasma parameter measurements for the V1 4-ring cusp configuration indicated that the electron density, ion density, and temperature had a primary peak on axis, as well as a secondary peak off axis, in the vicinity of the new magnetic cusp. The addition of the new cusp brought primary electrons and ions off of the centerline and created a radially uniform plasma in the cylindrical section. The V2 configuration also yielded a remarkably flat ion current density profile just upstream of the optics, which represents the optimum profile for an ion thruster in terms of minimizing grid wear and thrust vector losses. From the V1 case alone, it is unclear if the beam flattening effect was due to the migration of primary electrons off-axis or simply to the fact that the addition of the conical magnet ring pulled the field lines closer to the anode, increasing the field free volume.

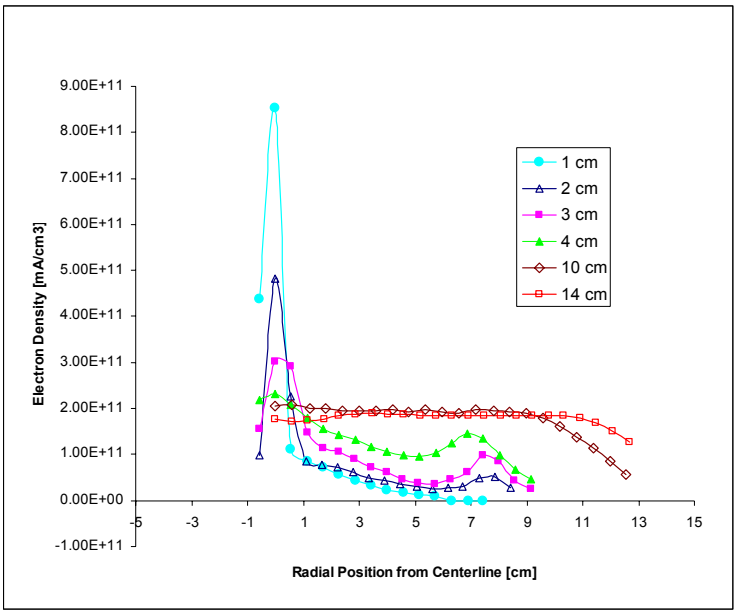

Figure 17. Electron Number Density Profiles at TH15 for V2 Configuration.

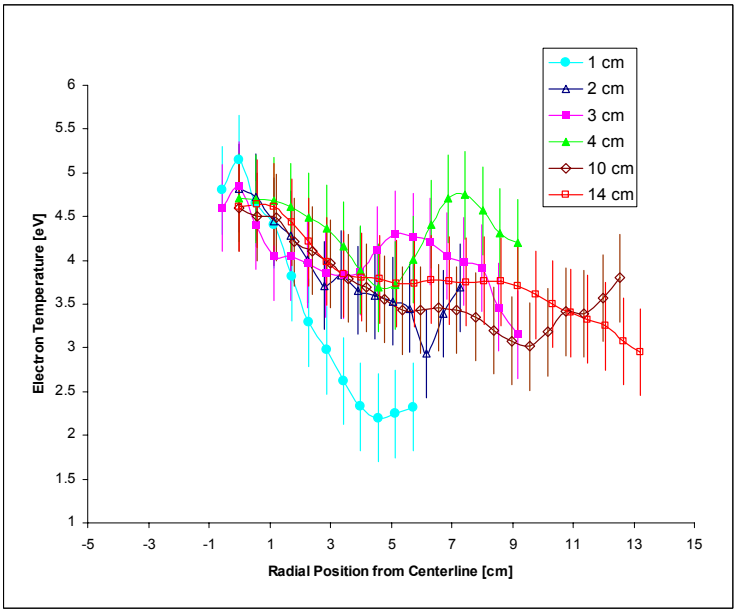

Figure 18. Electron Temperature Profiles at TH15 for V2 Configuration.

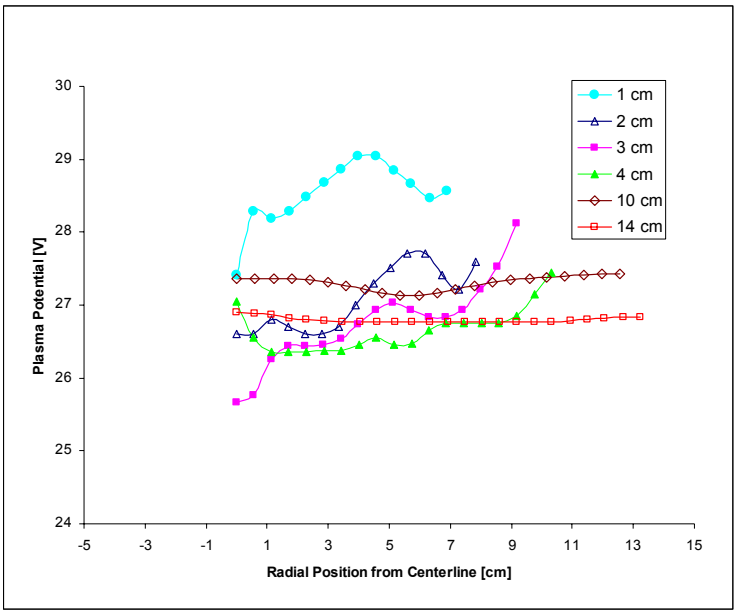

Figure 19. Plasma Potential Profiles at TH15 for V2 Configuration.

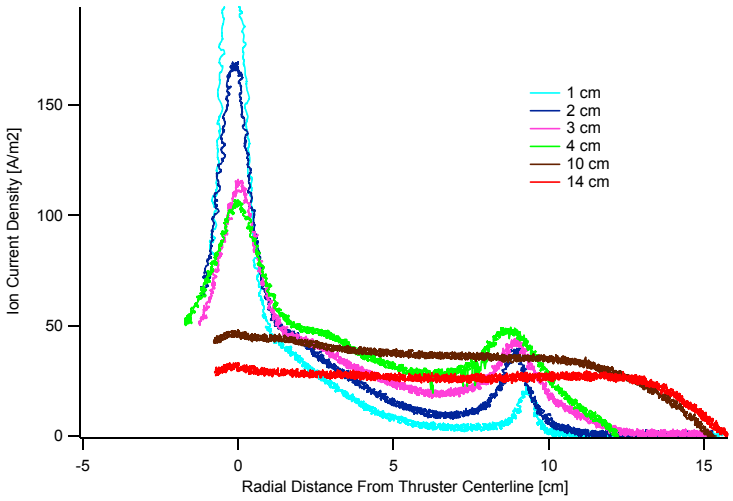

Figure 20. Ion Saturation Current Density Profiles at TH15 for V2 Configuration.

D. Enhanced 4 Ring Cusp NSTAR: Case V3

1. Overall Performance

DISCHARGE PARAMETER	NKO (V2)		
	TH15	TH8	TH0
J_B (A)	1.76	1.10	0.51
J_D (V)	11.5	7.3	4.3
V_D (V)	25.6	26.5	25
ε_b (V)	167.3	175.9	210.8
η_{tot}			

Table 5. 4-Ring Cusp V3 NSTAR Performance.

Case 3 is a 4-ring cusp modified NSTAR engine. In this configuration, in addition to the conical ring added in case 2, the middle magnet ring was strengthen by adding a ring of magnets to the interior of the discharge chamber, directly over the existing ring. The steel shim from case 2 was removed from the conical ring to reduce primary electron loss to this cusp. Removal of the shim increased the cusp strength to 1800 G as measured by a gauss-meter. Figure 22 and 23 are plots of the MAXWELL 2D predicted magnetic contour and field lines. This configuration closed the 50G contour throughout the chamber at the expense of reducing the field free volume in the cylindrical segment of the discharge chamber, specifically, just upstream of the optics. Primary electron loss is less than 10% in this configuration, due to the high strength cusps, therefore all gain in performance improvement can be attributed to enhanced ion confinement (reduced ion loss to the walls).

Table 5 is a performance summary of the V3 configuration. For TH15, the discharge current needed to produce 1.76A of beam current was only 11.5A, more than a 19% reduction from the nominal NSTAR configuration. This resulted in a discharge loss of 165 eV/ion, versus 210 eV/ion for the nominal NKO1 performance. Similar gains in discharge loss and total thruster efficiency were achieved for the throttled conditions as well. This confirms that increasing the value of the mimimum magnetic contour serves to magnetically confine ions, and reduce their loss to the walls. More detail on this mechanism will be discussed in the following sections.

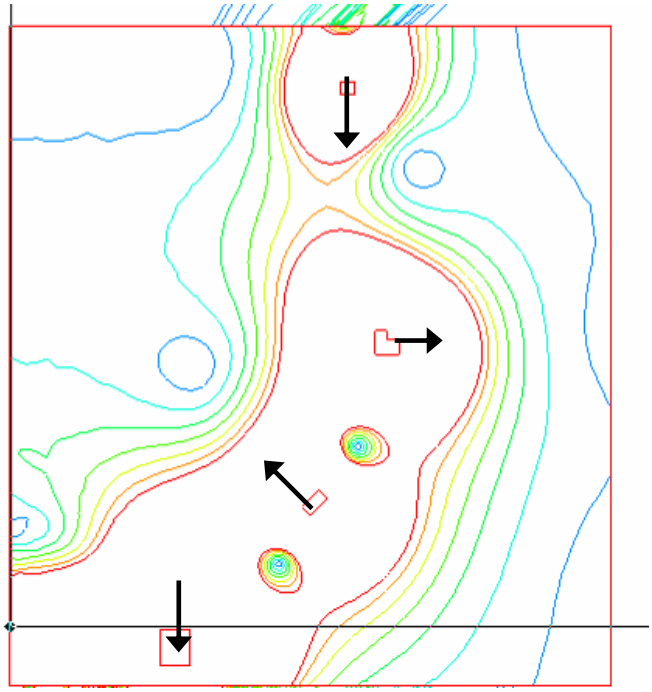

Figure 21. Magnetic Contours for Case V3.

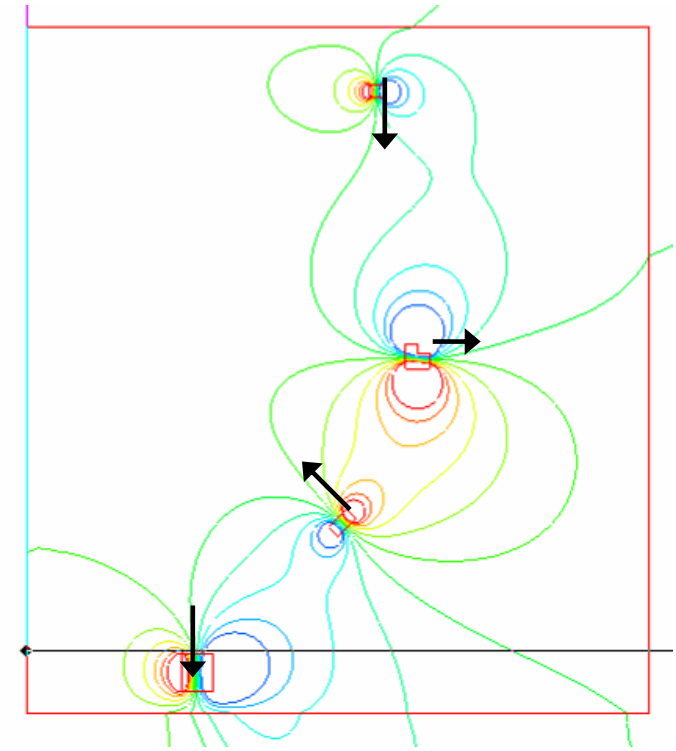

Figure 22. Magnetic Field Lines for Case V3.

2. Plasma Profiles

Radial plasma parameter profiles for case 3 were made with seven flat disk langmuir probes located at 1cm, 2 cm, 3cm, 4cm, 10cm, and 14cm axially with respect to the discharge cathode exit for the TH15 operating point. Each probe traversed from the anode wall to just past the centerline. TH15 operation is defined by the beam voltage, beam current, and flow rate setpoints in the NSTAR throttle table. Figure 23 is a plot of the electron number density. In the conical region of the discharge chamber, the radial variation in electron density had a primary peak on the centerline, with a secondary peak off axis. The primary peak, on the centerline had a maximum value of 4.5e11 cm^{-3}, as measured 1cm downstream of the cathode. The secondary peak was caused by the addition of the conical magnet ring, causing electrons to travel along the field lines to the new magnetic cusp. The maximum number density in the secondary peak was 1.75e11 cm^{-3}, 4cm radially from the centerline, as measured by the probe 4cm downstream of the cathode. The radial variation of electron density in the cylindrical region of the plasma decreased monotonically out to the anode wall. It varied from a maximum of 2e11 cm^{-3} on the centerline to 5e10 cm^{-3} near the anode wall. Figure 24 is a plot of electron temperature profiles in the discharge chamber. The radial variation of electron temperature in the conical segment, was peaked on axis (4.5 eV), with an additional off axis peak (3 eV), corresponding to the electron density peaks described previously. The electron temperature near the anode wall reached a minimum of 2.5eV in the conical segment. The electron temperature reached a minimum of 2 eV in the conical section, just radially in from the secondary peak, as measured by the 1, 2, and 3 cm axial position probes, suggesting that both primary and secondary electrons were tightly confined to the field lines terminating at the magnetic cusps. Radial variation, in the cylindrical segment was less peaked, and spanned 4 to 2.5 eV, with the maximum on the centerline, and minimum at the anode wall. Figure 25 is the plasma potential variation. The plasma potential structure in both the conical and cylindrical region of the discharge chamber, exhibited a radial trend of increasing potential with proximity to the anode wall. In the conical section, the plasma potential was roughly 26V on axis, and increased up to 32 V near the anode wall. In the cylindrical region of the chamber, the radial variation was relatively flat from the centerline out to 11cm. From 11 cm to the anode wall, however, the potential increased by 2 to 3V. Figure 26 represents the variation in ion saturation current density throughout the discharge chamber. For case V3, saturation current measurements were only made with a 500 Ohm current shunt, resulting in off scale centerline data for the 1, 2, and 3cm radial profiles in the figure. In the conical section, ion current density was highly peaked on axis, with a secondary peak off axis due to the new magnetic cusp. This behavior is identical to the

electron current density, confirming that the electrons electrostatically confine the ions, and quasineutrality is maintained throughout the plasma. In the near grid (cylindrical) region, ion density was peaked on the centerline, and exhibited a monotonically decreasing radial profile out to the anode. This behavior is markedly different than case 2, which had a uniform radial plasma profile. The increased magnetic field strength in this configuration reduced the field free region, which tends to make the plasma less uniform as it is more constrained.

The plasma parameter measurements for the v3 4-ring cusp configuration indicated that the electron density, ion density, and temperature had a primary peak on axis, as well as a significant secondary peak off axis, in the vicinity of the conical segment magnetic cusp. The addition of the new cusp brought electrons and ions off of the centerline and created a more radially uniform plasma in the cylindrical section. The addition of the strengthened middle magnet ring, increased ion confinement by allowing closure of the 50G contour line, and as a result the discharge loss decreased by 20% versus the nominal configuration. The strengthening of the middle magnet ring, did however, reduce the magnetic field free region in the cylindrical section and this resulted in a peaked ion current density profile just upstream of the optics. Although the beam profile was peaked, the magnitude of the current density peak was on the order of the nominal configuration, therefore V3 represents a dramatic improvement in performance and cathode life over the nominal NSTAR engine.

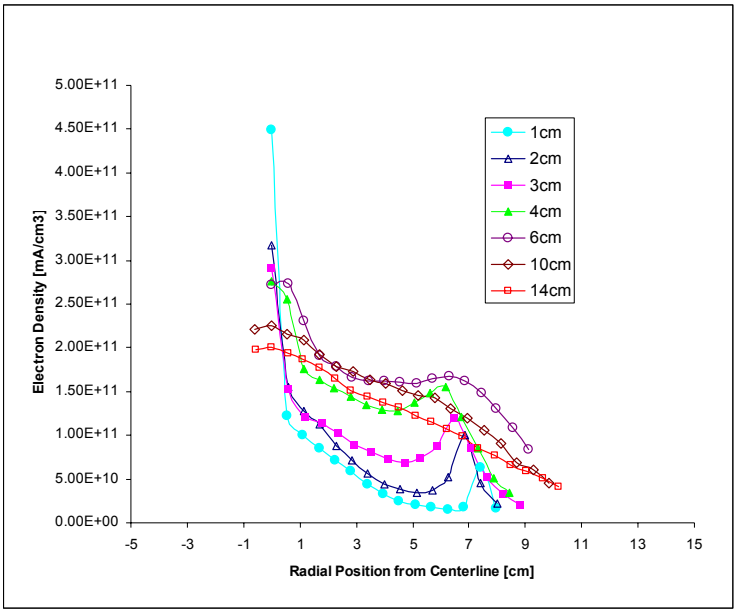

Figure 23. Electron Number Density Profiles at TH15 for V3 Configuration.

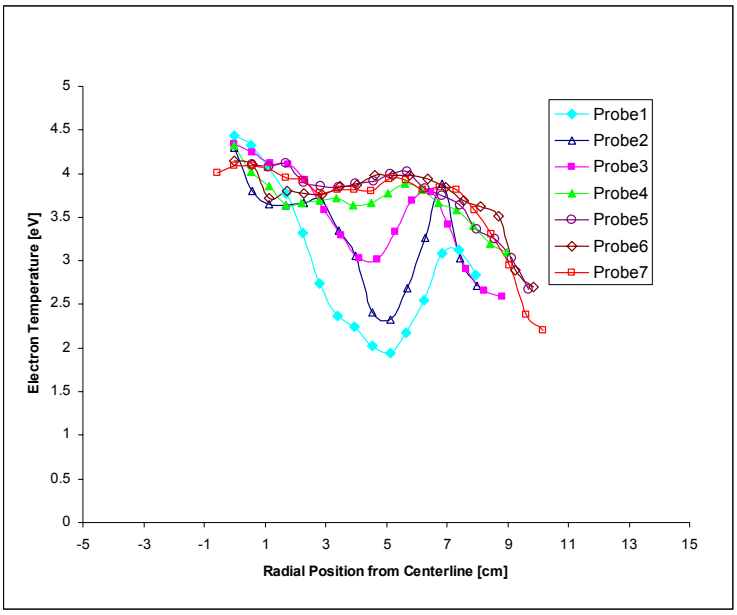

Figure 24. Electron Temperature Profiles at TH15 for V3 Configuration.

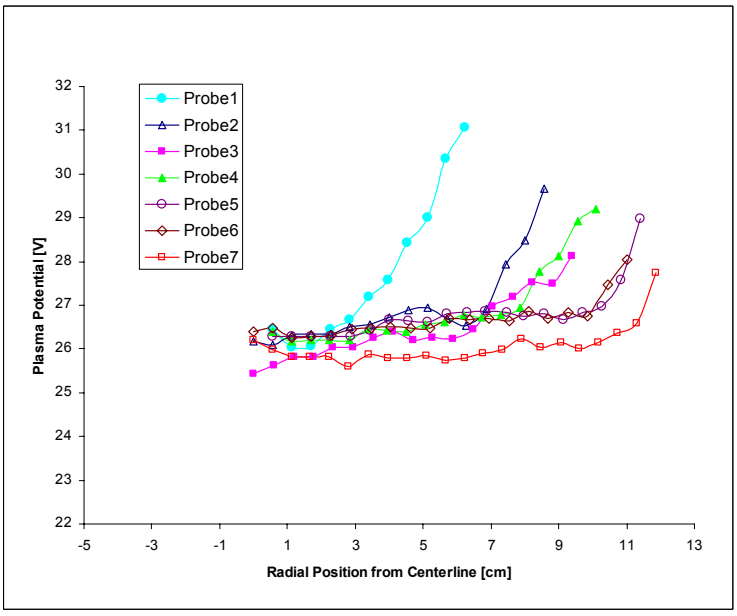

Figure 25. Plasma Potential Profiles at TH15 for V3 Configuration.

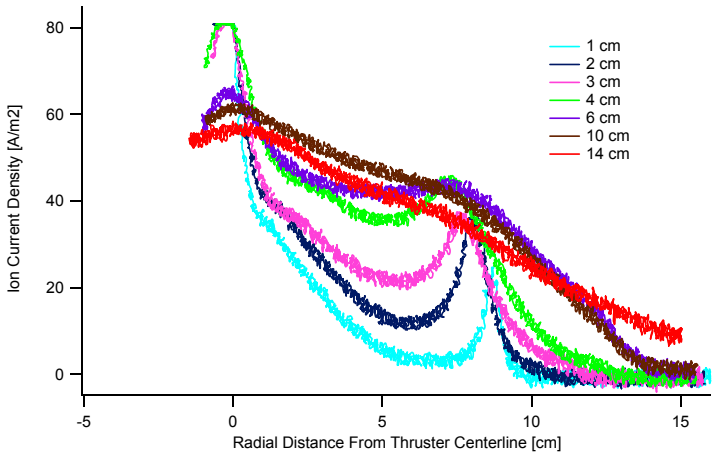

Figure 26. Ion Saturation Current Density at TH15 for V3 Configuration.

E. Enhanced 3 Ring Cusp NSTAR: Case V4

1. Overall Performance

Case 4 is an enhanced 3-ring cusp NSTAR engine. In this configuration, the conical ring from case 3 was removed, but the strengthened middle magnet ring was left in place. The cathode magnet ring polarity was reversed to allow for alternating polarity magnetic cusps. Figure 27 and 28 are plots of the MAXWELL 2D predicted magnetic contour and field lines. This configuration also closed the 50G contour throughout the chamber and the removal of the conical ring increased the field free volume throughout the chamber, as compared to case V3, where the field free volume was reduced. In addition, removal of the conical ring depressed the field line in the cylindrical segment, believed to be responsible for the peaked profile in case 3. This configuration was chosen separate the effects of increasing the closed contour line strength inside the chamber versus adding another cusp to drive primary electrons off axis. As long as the ions are adequately magnetically confined and the primary electron confinement length is sufficiently large to ensure an inelastic collision occurs prior to loss to the anode, it is believed that the addition of an additional cusp is not necessary.

Table 6 is a performance summary of the V4 configuration. For TH15, the discharge current needed to produce 1.76A of beam current was 11.6A, as compared to 11.3A for case v2, and 14.5 for the nominal case v1. The discharge loss for V4 was 165 eV/ion, versus 167 for case v3, a 21% reduction from the nominal NSTAR configuration. The slight improvement in discharge loss for v4 versus v3 was due to lower discharge voltage operation. Similar gains in discharge loss and total thruster efficiency were achieved for the throttled conditions as well, with a 10% and 19% reduction in discharge loss at TH8 and TH0 operation respectively.

DISCHARGE PARAMETER	NKO (V2)		
	TH15	TH8	TH0
J_B (A)	1.76	1.1	0.51
J_D (V)	11.6	7.5	4.5
V_D (V)	25.1	26.2	24.65
ε_b (V)	165.4	178.6	217.5
η_{tot}			

Table 6. 4-Ring Cusp V3 NSTAR Performance.

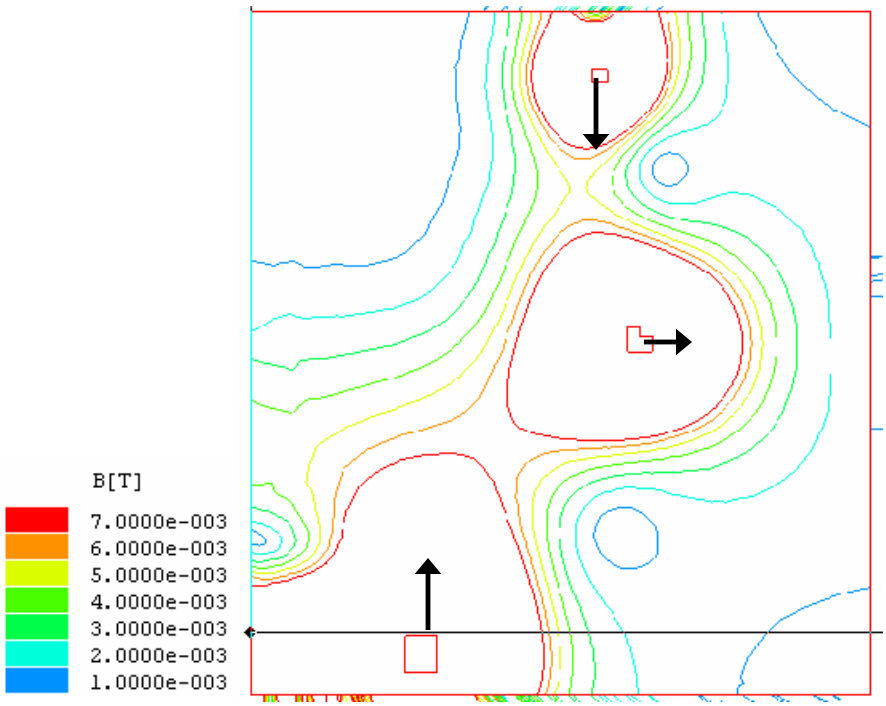

Figure 27. Magnetic Contours for Case V4.

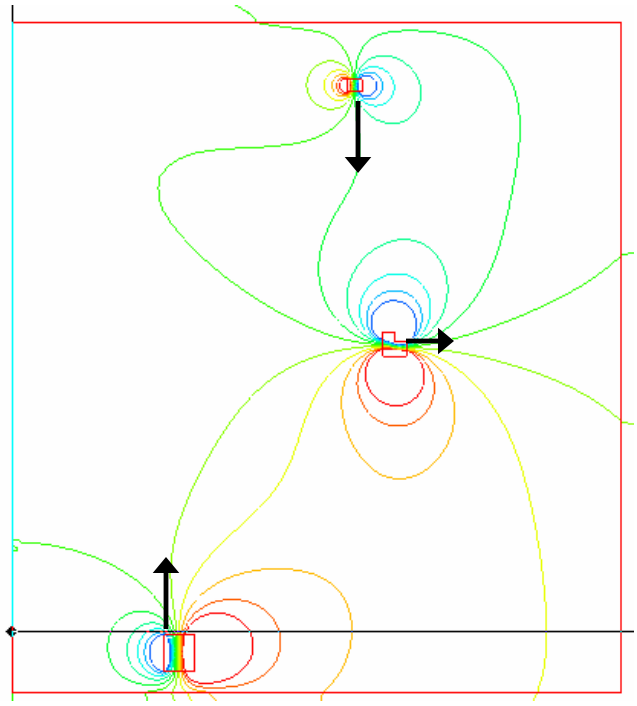

Figure 28. Magnetic Field Lines for Case V4.

2. Plasma Profiles

Radial plasma parameter profiles for case 4 were made with six flat disk langmuir probes located at 1cm, 2 cm, 3cm, 6cm, 10cm, and 14cm axially with respect to the discharge cathode exit. Figure 29 is a plot of the electron number density. In the conical region of the discharge chamber, the radial variation in electron density was highly peaked on the centerline. It reached a maximum value of 1.3e12 cm^{-3}, as measured 1cm downstream of the cathode on axis, and a minimum of 3e9 cm^{-3} at the anode wall in the conical segment. The radial variation of electron density in the cylindrical region of the plasma was relatively flat, from the centerline out to 8 cm radially, at 2e11 cm^{-3}. From 8 to 15 cm radially, the electron density decreased monotonically from 2e11 cm^{-3} to 9e9 cm^{-3}, near the anode wall. Figure 30 is a plot of electron temperature profiles in the discharge chamber. The $\pm$0.5 eV error bars are not shown on the figure for clarity. The radial variation of electron temperature in the conical segment, was peaked on axis (4.9 eV), and decreased monotonically to a minimum of 2.3 eV, near the anode wall. Variation, in the cylindrical segment was less peaked, and spanned 4.0 to 3.3 eV, from the centerline out to 8 cm radially. From 8cm to the anode wall the electron temperature decreased monatonically to a minimum of 2.4 eV. Figure 31 is the plasma potential variation for case v4. The plasma potential structure in the conical region of the discharge chamber decreased with axial distance from the cathode, by approximately 1V. As in case V3, the plasma potential increased with radial distance from the centerline, however, from 23V on the centerline, to 26V near the anode wall. In the cylindrical region of the chamber, the plasma potential was peaked on axis, but exhibited little radial variation outside of the cathode plume region out to 11 cm radially. The plasma potential increased from 11cm to the anode wall, from 23 to 26 V respectively. Figure 32 represents the variation in ion saturation current density, with the vertical scale expanded to show the ion density structure throughout the chamber. In the conical section, ion current density was highly peaked on axis, but became less peaked with axial distance from the cathode. In the near grid (cylindrical) region, ion density was flat from the centerline out to 11cm radially. From 11cm to 15cm the ion current density decreased monotonically to the anode wall. This behavior is different than case 3, which had a non-uniform beam profile from the centerline to the anode wall.

The plasma parameter measurements for the v4 3 ring cusp configuration indicated that the electron density, ion density, and temperature had a large primary peak on axis, and a non-uniform plasma in the conical region of the discharge chamber. However, in the cylindrical region, the plasma became more uniform, as the primary and secondary electrons were brought off axis in their transit to the strengthened middle magnet ring. The ion current density profiles show a significant flattening out, suggesting that ions are electrostatically confined to the electrons. Case v4 also had excellent performance, i.e. reduced ion loss to the walls, indicating that the 50G contour line closure is all that that is required to enhance ion confinement. The strengthening of the middle magnet ring without the conical cusp., increased the magnetic field free region in the cylindrical section and this resulted in a flat ion current density profile from the centerline out to 11cm, a dramatic improvement over case v3. In summary, V4 represents a dramatic improvement in performance and plasma uniformity, the implications of which will be discussed in the following section.

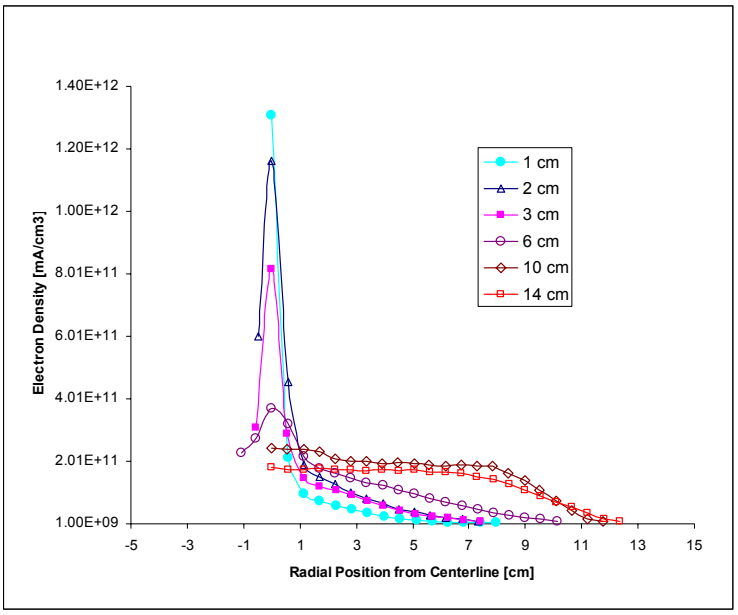

Figure 29. Electron Number Density at TH15 for V4 Configuration.

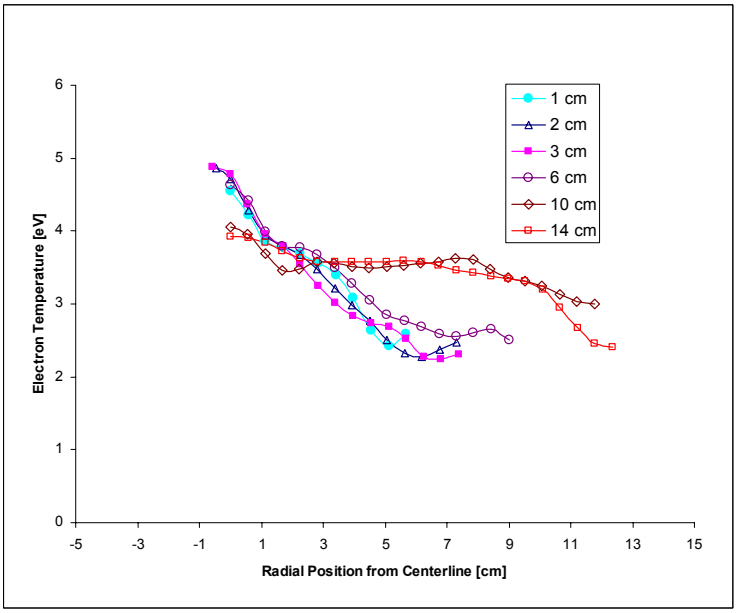

Figure 30. Electron Temperature at TH15 for V4 Configuration.

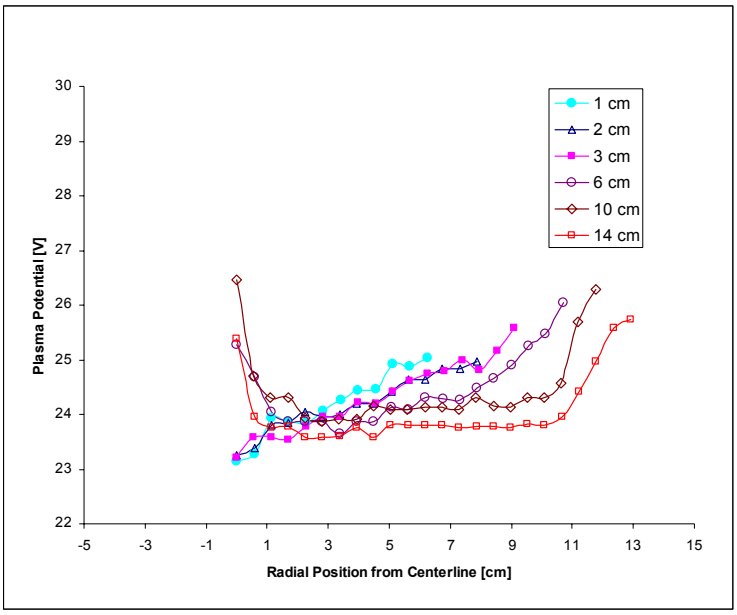

Figure 31. Plasma Potential at TH15 for V4 Configuration.

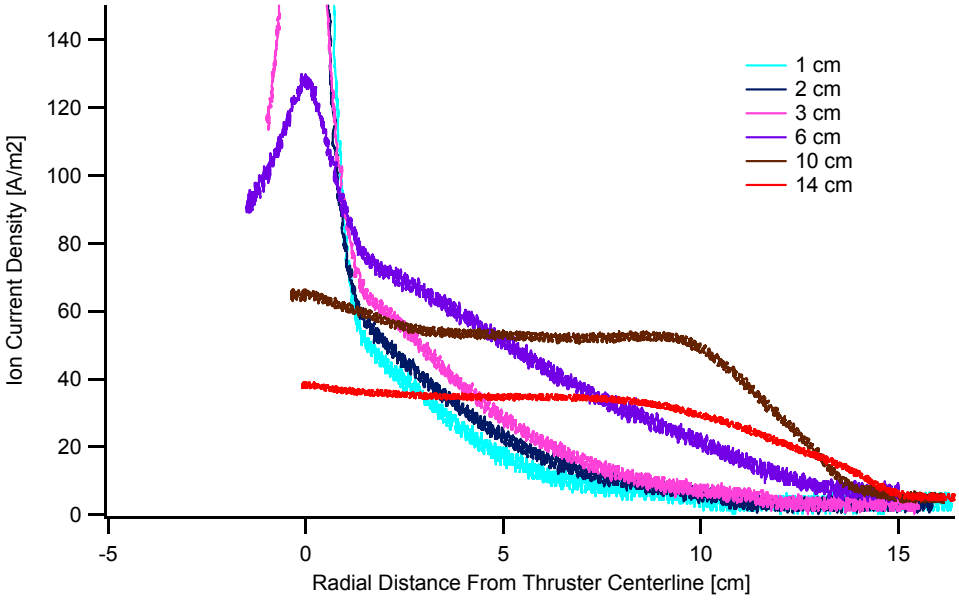

Figure 32. Ion Current Density at TH15 for V4 Configuration.

IV. Discussion

The magnetic confinement studies yielded several important findings. First, is it clear from the four cases tested, that improving ion confinement is the key mechanism for improving the electrical efficiency of the NSTAR thruster. In the nominal configuration up 35% of all ions producesd are lost to the anode wall. Cases V3 and V4 have demonstrated that ion loss can be reduced to 10% by increasing the value of the minimum closed contour. The magnetic confinement of ions is due to the requirement of quasineutrality in the discharge chamber. As electrons are more mobile than ions, wherever the electrons go, the ions will follow. The mechanism for confining primary electrons is to simply have sufficiently strong magnetic cusps, such that they are confined to the field lines and will undergo an inelastic collision prior to being lost to the cusps. For low energy electron confinement, it is necessary to prevent radial diffusion. Such diffusion can be represented by random walk of the charged particle in the direction opposite the density gradient[11]. For random walk across a magnetic field, as is the case in an ion thruster, the diffusive path length or mean free path between collisions, is defined by the larmor radius. Therefore minimizing electron diffusion is simply a function of the magnetic field strength. As ions are electrostatically confined by the electrons, or by electric fields setup by deficits (or surpluses) of charge, the ions will be confined due to the requirement of quasineutrality. The plasma density and potential profiles for the cases investigated support this theory. In the cases where ion confinement was enhanced, the plasma potential near the anode wall increased in value, setting up an electric field that retards ions. In the cases where ion confinement was poor, there was no radial gradient in potential in the anode region. Similarly, the ion density throughout the chamber was equivalent to the electron density, suggesting that the plasma is quasineutral throughout, and that ions do indeed follow electrons.

Improving plasma uniformity in the near grid plasma does not appear to be related to plasma uniformity in the conical region of the plasma however. In fact, case V3, which had the most uniform conical region plasma, due to the addition of the conical cusp, had the least radially uniform plasma profile in the near grid region. Plasma uniformity in the near grid region is primarily a function of the magnetic field structure in this region. Increasing the field free volume is critical for producing a flat beam profile. Figure 33 and 34 are comparative plots of ion current density for the four cases investigated. Figure 33 is the beam profile, or the scan that was taken 14cm downstream of the cathode (2cm upstream of the screen grid). Case V2 has a completely flat beam profile, versus V3 which is peaked on axis. Figure 34 is ion current density taken at 6cm downstream of the cathode. Here V3 has the flattest beam profile, and V4 the most peaked. Therefore it is clear that the plasma distribution in the conical region did not affect the beam profile.

In addition to the performance and total efficiency improvement obtained by reducing the discharge loss by 20%, there are lifetime enhancements for the NSTAR thruster. Emitter life has an exponential dependence of insert temperature or current density[2]. Therefore utilizing the depletion rate coefficients developed by reference [2], operation at 11.3 versus 14.3 A, increases cathode life, from the perspective of barium depletion, by 45%, from 43khrs to 62khrs for TH15 operation. Similarly, by reducing the peak current density by flattening out the beam profile, grid life can be increased by 20% over the nominal configuration[3].

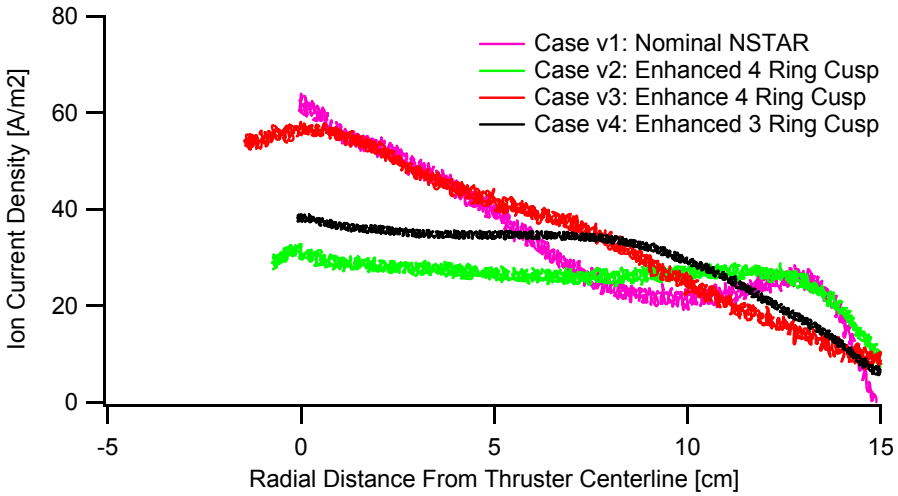

Figure 33. Ion Current Density Comparison for 14cm downstream of keeper (near grid region)

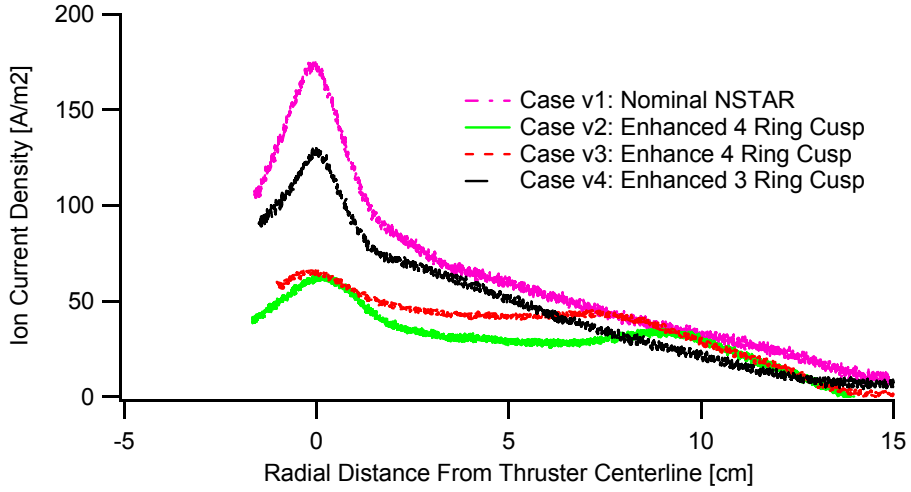

Figure 34. Ion Current Density Comparison for 6 cm downstream of keeper (conical region).

V. Conclusion

The objective of this research was to use a combined approach of theoretical development of the discharge plasma confinement theory in conjunction with spatially resolved experimental measurements inside of an operating ion thruster, to quantitatively understand and improve upon the confinement and production of the discharge plasma. The experimental investigationsserved to map out the plasma structure and its confinement as a function of various magnetic field geometries. The end result of the research activity was to experimentally validate an enhanced NSTAR thruster design that improves ionization efficiency by 20%, plasma uniformity by 25%, significantly increasing the efficiency and lifetime of the NSTAR thruster. Such an improvement in performance and throughput of the NSTAR thruster was easily accomplished via a straightforward change in the magnetic field.

Acknowledgments

The authors would like to acknowledge Dan Goebel, Ray Swindlehurst, and Rob Kolasinski, of the Jet Propulsion Laboratory, who assisted in the test preparation and conduct of this research. Jet Propulsion Laboratory, California Institute of Technology carried out the research described in this paper, under a contract with the National Aeronautics and Space Administration..

References

[1] Sengupta, A., et al, "Overview of the Results from the 30,000 Hr Life Test of the Deep Space 1 Flight Spare Ion Engine," AIAA-2004-3608, 40th Joint Propulsion Conference, Fort Lauderdale, FL, July 2004.

[2] Palluel, P., and Shroff, A. M., "Experimental Study of Impregnated Cathode Behavior, Emission, and Life," *J. Appl. Phys.* 51(5), May 1980.

[3]Katz,I., et.al., "CEX 2D Modeling Reference"

[4]Herman, D., et al., "Comparison of Discharge Plasma Parameters in a 30-cm NSTAR Type Ion Engine with and without Beam Extraction", AIAA-03-5162, July, 2003.

[5]Sengupta et. al., "Experimentally Determined Neutral Density and Plasma Parameters in a 30cm Ion Engine," AIAA-2004-3613.

[6] Sengupta, A., et al, "The 30,000-Hr Life Test of the DS1 Flight Spare Ion Thruster, Final Report," NASA/TP 2004-213391.

[7]Godyak, R.B., et. al., "Probe Diagnostics of Non-maxwellian plasmas", J. Applied Phys., 73 (8), 15 April 1998.

[8]Williams, G. J., et al., "Characterization of Discharge Cathode Plume," IEPC Paper, 27th International Electric Propulsion Conference, Pasadena, CA, Oct. 2001.

[9]Sudit, I.D., Woods, R.C., "A study of the Accuracy of Various Langmuir Probe Theories", J.Appl. Phys. 76 (8) 1995.

[10]Clements, R.M., "Plasma Diagnostics With Electric Probes", J. Vac. Sci. Technol., 15 (2), Aprik 1978.

[11]Chen, F.F., "Introduction to Plasma Physics and Controlled Fusion", Second Edition, Plenun Press, New York, 1984.

[12]Laframboise, J.G., "Theory of Spherical and Cylindrical Langmuir Probes in a Collionless, Maxwellian Plasma At Rest", UTIAS Report No. 100, June 1966.
[13]Huddlestone, "Plasma Diagnostic Techniques", Ch 4,.
[14]Goebel, D.M., et. al., "Hollow Cathode and Keeper-Region Plasma Measurements Using Ultra-Fast Miniature Scanning Probes", Joint Propulsion Conference, Fort Lauderdale FL, July 10th -13th, 2004
[15]Sengupta, A., et al, "Status of the Extended Life Test of the Deep Space 1 Flight Spare Ion Engine After 30,352 Hours of Operation," AIAA-2003-4558, July 2003.
[16]Kolasinski, R. D., and Polk, J. E., "Characterization Of Cathode Keeper Wear By Surface Layer Activation," AIAA-2003-5144, July, 2003.
[17]Williams, G. J., et al., "Characterization of FMT-2 Discharge Cathode Plume," IEPC Paper #99-104, 26th International Electric Propulsion Conference, Ketakiushu, Japan, Oct. 1999.
[18]Polk, J. E., et al., "An Overview of the Results from an 8200 Hour Wear Test of the NSTAR Ion Thruster," AIAA-99-2446, June 1999.